Journal of Magnetism and Magnetic Materials 441 (2017) 124–130

Contents lists available at ScienceDirect

Journal of Magnetism and Magnetic Materials

journal homepage: www.elsevier.com/locate/jmmm

Research articles

Revealing the transport properties of the spin-polarized β′-$Tb_2(MoO_4)_3$: DFT+U

A.H. Reshak *

New Technologies – Research Centre, University of West Bohemia, Univerzitni 8, 306 14 Pilsen, Czech Republic
School of Material Engineering, University Malaysia Perlis, 01007 Kangar, Perlis, Malaysia

ARTICLE INFO

Article history:
Received 7 February 2017
Received in revised form 11 April 2017
Accepted 20 May 2017
Available online 22 May 2017

Keywords:
Electronic materials
Inorganic compounds
Ab initio calculations
Band-structure
Transport properties

ABSTRACT

The thermoelectric properties of the spin-polarized β′-$Tb_2(MoO_4)_3$ phase are calculated using first-principles and second-principles methods to solve the semi-classical Bloch-Boltzmann transport equations. It is interesting to highlight that the calculated electronic band structure reveals that the β′-$Tb_2(MoO_4)_3$ has parabolic bands in the vicinity of the Fermi level (E_F); therefore, the carriers exhibit low effective mass and hence high mobility. The existence of strong covalent bonds between Mo and O in the MoO_4 tetrahedrons is more favorable for the transport of the carriers than the ionic bond. It has been found that the carrier concentration of spin-up (↑) and spin-down (↓) increases linearly with increasing the temperature and exhibits a maximum carrier concentration at E_F. The calculations reveal that the β′-$Tb_2(MoO_4)_3$ exhibits maximum electrical conductivity, minimum electronic thermal conductivity, a large Seebeck coefficient and a high power factor at E_F for (↑) and (↓). Therefore, the vicinity of E_F is the area where the β′-$Tb_2(MoO_4)_3$ is expected to show maximum efficiency.

1. Introduction

Molybdate crystals have become considerable candidates for practical applications in photonic, laser, thermoelectric and electronic technologies [1–8]. Because the rare-earth ions occupy low-symmetry positions, the molybdates containing rare-earth ions gain special attention as laser and luminescent hosts [6,8–16]. It is interesting to mention that rare-earth molybdates can be obtained in the form of large single crystals of high optical quality, characterized by high mechanical resistance, great resistance to external factors, and interesting elastic and electric properties [17]. One of the important rare-earth molybdates candidates is terbium molybdate in β′-phase, β′-$Tb_2(MoO_4)_3$ (β′-TMO). β′-TMOs are fully coupled ferroelectric-ferroelastic crystals; these are well-known materials in addition to $Gd_2(MoO_4)_3$ [18,19]. Peng et al. [20] investigated the transmission spectrum of β′-TMO and found that it is transparent over the range of about 340–1750 nm, with an energy band gap of about 3.76 eV and a large absorption peak at 486 nm. They measured the photoluminescence of the $Tb_2(MoO_4)_3$ and observed the peaks at 490 nm, 540 nm, 580 nm and 615 nm, which are attributed to the electronic transitions of Tb^{3+} ions. The strongest photoluminescence intensity is excited by the light of 486 nm, which is mainly caused by the energy absorption at 486 nm indicated in the transmission spectrum. The molybdates possess a sequence of the phase transitions with a temperature variation, and the β and β′ polymorph modifications are noncentrosymmetric [21–25]. Recently, MoO^{3-} based crystals such as $ZnMoO_4$ and KLa $(MoO4)_2$ have been reported to be good hosts for Tb^{3+} doping and green emission [26,27].In our previous work [28], we performed spin-polarized calculations to investigate the ground state properties of the β′-$Tb_2(MoO_4)_3$ using the density functional theory plus *U*-Hubbard Hamiltonian. In this report, we will reveal the influence of the spin-polarization on the transport properties. Therefore, as a step forward to understand the origin of the conductivity in the β′-$Tb_2(MoO_4)_3$, we have performed comprehensive theoretical investigations based on the all-electron full-potential method within the semi-classical Boltzmann theory as incorporated in the BoltzTraP code to calculate the transport properties of the β′-$Tb_2(MoO_4)_3$. Simulations of the thermoelectric properties are a transition from first- to second-principles methods. The first-principles method used here is the all-electron full-potential linear augmented plane wave (*FPLAPW + lo*) method [29], whereas the second-principles method is the BoltzTraP code [30], which solves the semi-classical Bloch-Boltzmann transport equations within the constant relaxation time approximation.

The transport properties can provide detailed information about the electronic structure of the materials. The transport properties

* Address: New Technologies – Research Centre, University of West Bohemia, Univerzitni 8, 306 14 Pilsen, Czech Republic.
E-mail address: maalidph@yahoo.co.uk

http://dx.doi.org/10.1016/j.jmmm.2017.05.060
0304-8853/

of solids are a major topic, both in basic research as well as for industrial applications. While for the former the origin and nature of different excitation processes is of fundamental interest, the latter can make use of them in many thermoelectric devices.

2. Details of calculations

The β′-$Tb_2(MoO_4)_3$ phase crystallizes in orthorhombic symmetry with the Pba2 space group at temperatures below 433 K [24,25]. The experimental lattice parameters are a = 10.35387 (6) Å, b = 10.38413(6) Å, c = 10.65695(7) Å and V = 1145.79(1) $Å^3$ [31]. It is known that three different types of $(MoO4)^{2-}$ tetrahedrons having different mean distances of Mo–O bonds are present in the β′-$RE_2(MoO_4)_3$ crystals, i.e., type-I, II, and III; three crystallographically independent $(MoO_4)^{2-}$ tetrahedra form successive layers along the c-axis [32–35]. Each $(MoO_4)^{2-}$ tetrahedron is discrete, and each oxygen atom in $(MoO_4)^{2-}$ is bonded only to one Mo atom, in addition to either one or two Tb atoms (Fig. 1). The O atoms of the MoO_4 tetrahedrons form strong covalent bonds with Mo atoms, while the O atoms in TbO_7 polyhedrons forms very weak covalent bonds, as is confirmed by the interatomic distances between Tb-O and Mo-O [31]. Covalent bonding is more favorable for the transport of the carriers than ionic bonding [36].The full-potential linear augmented plane wave plus the local orbitals ($FPLAPW + lo$) method, as implemented in the WIEN2k code [29] within the generalized gradient approximation ($PBE - GGA$) [37], was used to optimize the experimental structural geometry of the β′-$Tb_2(MoO_4)_3$ compound [31]. The optimized crystal structure of the β′-$Tb_2(MoO_4)_3$ is depicted in Fig. 1; the structure consists of MoO_4 tetrahedrons and TbO_7 polyhedrons linked by corners. It is well known that for oxides and other highly correlated compounds the electrons are highly localized. Therefore, the local density approximation (LDA) and GGA fail to give the correct ground state. The Coulomb repulsion between the electrons in open shells should be taken into account. Therefore, it has been proposed that a simpler approach is to add the Hubbard-like on-site repulsion to the Kohn-Sham Hamiltonian, which is called DFT + U (U-Hubbard Hamiltonian). From the obtained relaxed geometry, the ground state properties were determined using $FPLAPW + lo$ [37–41] within GGA+U. We applied U on the 4*f* orbital of Tb atoms and the 4*d* orbital of Mo atoms; several U values were used until we reached the U values that give a result in concordance with experimental data. The U values used here are 0.54 Ry and 0.22 Ry for the Tb-4f and Mo-4d, respectively.

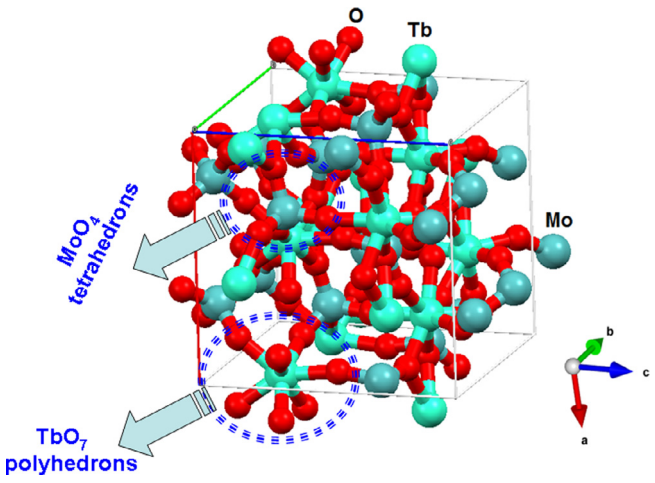

Fig. 1. Crystal structure of β′-$Tb_2(MoO_4)_3$, the MoO_4 tetrahedrons and TbO_7 polyhedrons are linked by corners, MoO_4 tetrahedrons in β′-$Tb_2(MoO_4)_3$, TbO_7 polyhedrons in β′-$Tb_2(MoO_4)_3$.

The spin-polarized transport properties of the β′-$Tb_2(MoO_4)_3$ are obtained utilizing the semi-classical Boltzmann theory as incorporated within the BoltzTraP code [30]. The calculations of the transport properties are a transition from first- to second-principles methods. The first-principles method used here is the FPLAPW+lo, whereas the second-principles method is the BoltzTraP code [30]. In the BoltzTraP code, the semi-classical Bloch-Boltzmann transport equations are solved within the constant relaxation time approximation [30].The potential for the construction of the basis functions inside the sphere of the muffin-tin was spherically symmetric, whereas it was constant outside the sphere. Self-consistency is obtained using 800 $\overline{K}$ points in the irreducible Brillouin zone (*IBZ*). The self-consistent calculations are converged since the total energy of the system is stable within 0.00001 Ry. The spin-polarized transport properties were calculated within 1728 $\overline{K}$ points in the *IBZ*. It is well known that first-principles calculations are a powerful and useful tool to predict the crystal structure and its properties related to the electron configuration of a material before its synthesis [42–44].

3. Results and discussion

3.1. Salient features of the spin-polarized electronic band structure

The spin-polarized electronic band structure for spin-up (↑) and spin-down (↓) are calculated and illustrated in Fig. 2 (a and b), to investigate the influence of the spin-polarization on the transport properties of the β′-$Tb_2(MoO_4)_3$. The (↑) and (↓) channels exhibit an indirect energy band gap as the valence band maximum (VBM) is located at Y point of the BZ and the conduction band minimum (CBM) at the center of the BZ. The zero of the energy scale is taken at the top of the valence band for both spins. It has been found that the calculated values of the band gap is 3.61 eV for (↑) and (↓), in close agreement with the measured one (3.76 eV) [45–48]. It is clear that the electronic band structures of the β′-$Tb_2(MoO_4)_3$ for (↑) and (↓) channels present identical structures; therefore, the spins display similar characteristics in all regards. To ascertain this observation, we have presented the necessary ingredients of the calculated total density of states as shown in Fig. 2 (a and b), which show that the total density of states (TDOS) for (↑) and (↓) channels are identical, confirming that the spin-polarization has identical influence on the ground state properties of the β′-$Tb_2(MoO_4)_3$. We enlarged the electronic band structure in the area around the CBM and the VBM; we found that both the CBM and VBM have parabolic bands in the vicinity of the Fermi level (Fig. 2(c and d). This implies that the β′-$Tb_2(MoO_4)_3$ – shows the highest **k**-dispersion bands around E_F and thus the lowest effective masses and the highest mobility carriers.

3.2. Spin-polarized thermoelectric properties

The influence of the temperature on the carrier concentration (n) of the β′-$Tb_2(MoO_4)_3$ for (↑) and (↓) channels is investigated. Fig. 3(a) shows that at a certain value of the chemical potential, the (↑) and (↓) n increases linearly with increasing the temperature (T). When we vary the chemical potential ($\mu - E_F$) between −0.4 and +0.4 eV, the (↑) and (↓) n at three constant temperatures (300, 600 and 900 K) in the vicinity of E_F is obtained, as illustrated in Fig. 3(b and c). The difference between μ and E_F is positive for VB's and negative for CB's. It is clear from the electronic band structure (Fig. 2 (c and d)) that β′-$Tb_2(MoO_4)_3$ has parabolic bands in the vicinity of E_F;therefore, the carriers exhibit low effective mass and hence high mobility. It has been found that the β′-$Tb_2(MoO_4)_3$ exhibits a maximum n in the vicinity of E_F. To gain high thermoelectric efficiency, it is necessary that the material possesses high electrical

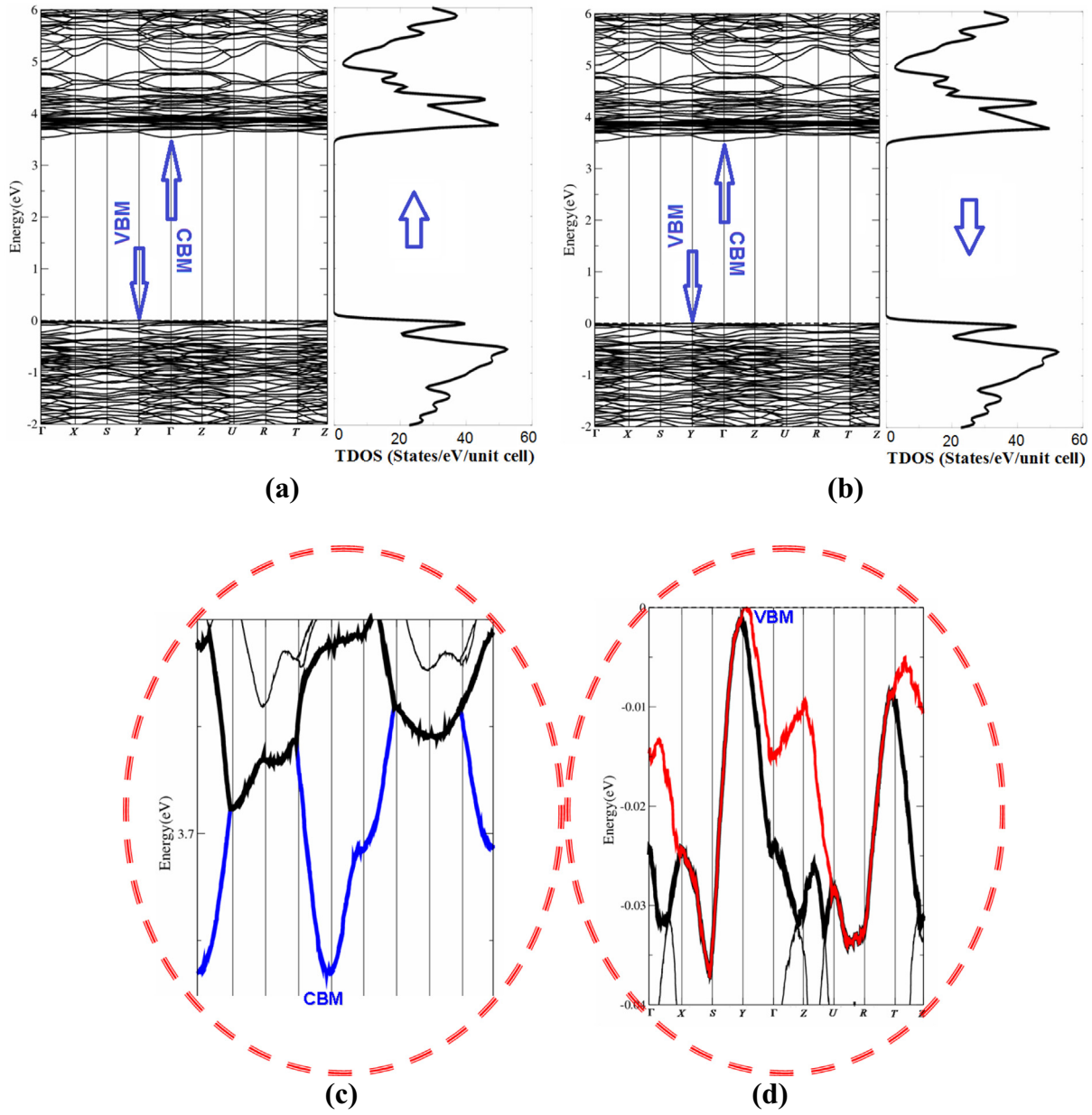

Fig. 2. Calculated electronic band structure along with the total density of states for β′-$Tb_2(MoO_4)_3$: **(a)** Spin-up; **(b)** Spin-down; **(c)** enlarged area of the electronic band structure around CBM; **(d)** enlarged area of the electronic band structure around VBM.

conductivity (σ/τ), a large Seebeck coefficient and low thermal conductivity (k_e/τ) [49]. Therefore, to achieve the highest σ/τ, high mobility carriers are required. To achieve this, a material with small effective masses is needed. Therefore, we have calculated the effective mass from the calculated band structure of the β′-$Tb_2(MoO_4)_3$ for (↑) and (↓) channels. The calculated electron effective mass ratio (m_e^*/m_e) around Γ point of the BZ is about 0.0524, whereas the effective mass ratio of the heavy holes (m_{hh}^*/m_e) around Y point of the BZ (Fig. 2(d)) is about 0.1557. This implies that heavy holes possess lower mobility than the electrons. To ascertain that the β′-$Tb_2(MoO_4)_3$ can be expected to give maximum efficiency at the vicinity of E_F, we investigated σ/τ as a function of chemical potential ($\mu - E_F = \pm 0.3$ eV) at three T values, as shown in Fig 3(d). It was noticed that the β′-$Tb_2(MoO_4)_3$ shows the maximum σ/τ at the vicinity of E_F for (↑) and (↓), the area where the β′-$Tb_2(MoO_4)_3$ expected to show maximum efficiency. The maximum value is found to be around $\pm 5.3 \times 10^{24}$ $(\Omega ms)^{-1}$ for (↑) and (↓) at 300 K, which is significantly reduced with increasing T. It is clear that there is a significant influence on σ/τ when we vary $\mu - E_F$ between -0.3 and + 0.3 eV. Therefore, the investigated compound possesses noticeable σ/τ at the vicinity of E_F. The calculated (↑) and (↓) σ/τ are presented in Table 1. Furthermore, we investigated the influence of increasing the temperature on σ/τ for both channels at a certain value of chemical potential as shown in Fig. 3(e). It was noticed that at temperatures up to 400 K, σ/τ increases significantly with rising T. Above 400 K, σ/τ shows insignificant response to T to reach its maximum value at 900 K.

3.2.1. Electronic thermal conductivity

Thermal conductivity (k) consists of electronic contribution k_e (electrons and holes transporting heat) and phonon contribution k_l (phonons traveling through the lattice). The BoltzTraP code calculates only the electronic part k_e [30]. Using the BoltzTraP code, we calculated k_e/τ of the β′-$Tb_2(MoO_4)_3$ for (↑) and (↓) as a function

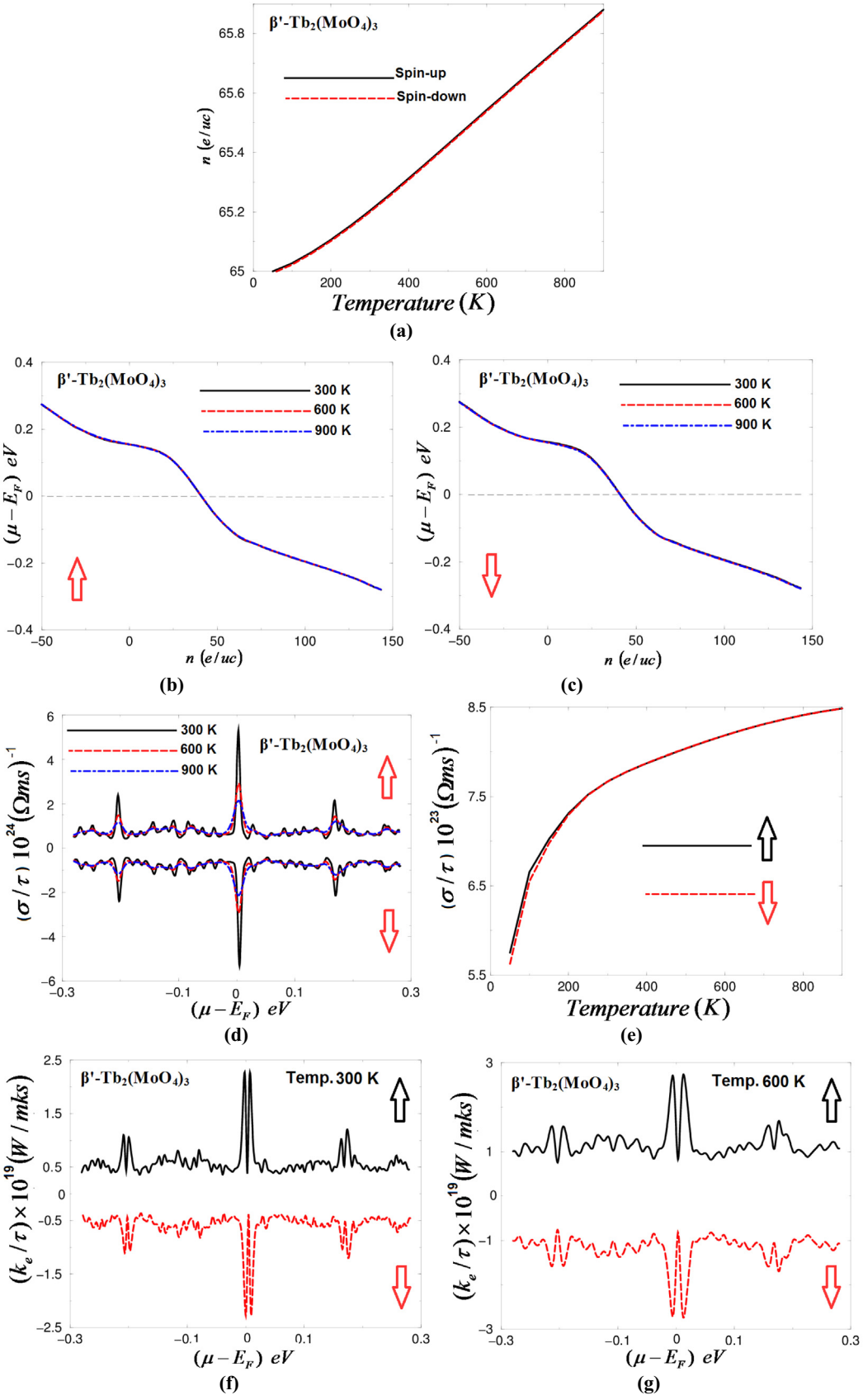

Fig. 3. Calculated transport properties for spin-up and spin-down for β′-$Tb_2(MoO_4)_3$; **(a)** The temperature induced n per unit cell (e/uc) for (↑) electrons versus T for β′-$Tb_2(MoO_4)_3$; **(b, c)** calculated (↑)(↓) n as a function of chemical potential ($\mu - E_F = \pm 0.4$ eV) at 300, 600 and 900 K for β′-$Tb_2(MoO_4)_3$; **(d)** The (↑)(↓) σ/τ of β′-$Tb_2(MoO_4)_3$ as a function of $\mu - E_F = \pm 0.3$ eV at 300, 600 and 900 K; **(e)** The (↑)(↓) $\sigma/\tau$of β′-$Tb_2(MoO_4)_3$ as a function of T at a certain value of the chemical potential; **(f-h)** The (↑)(↓) $k_e/\tau$of β′-$Tb_2(MoO_4)_3$ as a function of $\mu - E_F = \pm 0.3$ eV at 300, 600 and 900 K; **(i)** The electronic (↑)(↓) k_e/τ versus T for β′-$Tb_2(MoO_4)_3$; **(j)** The Seebeck coefficient for spin-up/down electrons versus temperature for β′-$Tb_2(MoO_4)_3$; **(k–m)** The (↑)(↓) S of β′-$Tb_2(MoO_4)_3$ as a function of $\mu - E_F = \pm 0.15$ eV at 300, 600 and 900 K; **(n)** The (↑)(↓) P versus T for β′-$Tb_2(MoO_4)_3$; **(o–q)** The (↑)(↓) P of β′-$Tb_2(MoO_4)_3$ as a function of $\mu - E_F = \pm 0.15$ eV at 300, 600 and 900 K.

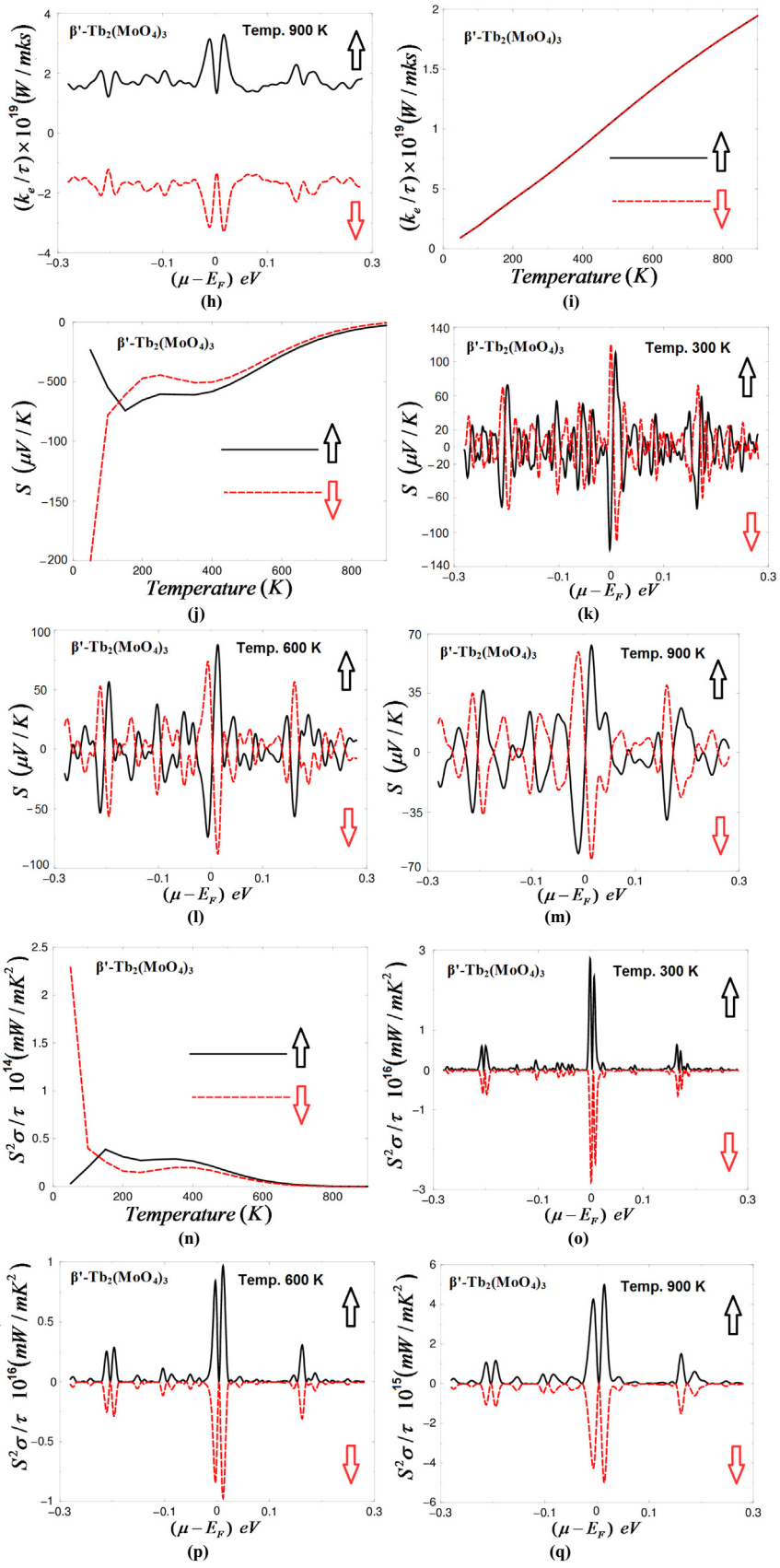

Fig. 3 (*continued*)

Table 1
Calculated values of (↑)(↓) $\sigma/\tau(\Omega ms)^{-1} \times 10^{24}$, (↑)(↓)$k_e/\tau(W/mks) \times 10^{19}$, (↑)(↓) S ($\mu V/K$) and (↑)(↓)$P(W/mk^2s) \times 10^{16}$.

	Electrical conductivity $(\Omega ms)^{-1} \times 1024$			Thermal conductivity$(W/mks) \times 1019$			Seebeck coefficient ($\mu V/K$)			Power factor $(W/mk^2s) \times 1016$		
	300 K	600 K	900 K	300 K	600 K	900 K	300 K	600 K	900 K	300 K	600 K	900 K
Spin-up	5.33	2.83	2.10	2.28, 2.28	2.76, 2.76	3.19, 3.36	110, −120	88.7, −74.6	64.7, −60.4	2.81, 2.35	8.40, 9.81	0.436, 0.504
Spin-down	−5.38	−2.89	−2.18	−2.25, −2.25	−2.70, −2.76	−3.13, −3.28	119, −109	72.2, −88.7	61.1, −64.0	−2.84, −2.35	−8.54, −9.62	−0.42, −0.50

of chemical potential ($\mu - E_F = \pm 0.3$ eV) at three T values, as shown in Fig 3(f–h). It was noticed that the β′-$Tb_2(MoO_4)_3$ shows the minimum k_e/τ at the vicinity of E_F, the area where β′-$Tb_2(MoO_4)_3$ is expected to exhibit maximum efficiency. Materials with low k are favorable for designing efficient thermoelectric devices, in which it is important to maintain the temperature gradient. Also, it was noticed that the β′-$Tb_2(MoO_4)_3$ exhibits a maximum k_e/τ just above and below E_F. There is a significant increase in the observed k_e/τ with increasing T along $\mu - E_F = \pm 0.3$ eV. To ascertain this behavior, we calculated the k_e/τ of the β′-$Tb_2(MoO_4)_3$ for (↑) and (↓) at a certain value of chemical potential as a function of T, as shown in Fig. 3(i). It is clear that k_e/τ increases linearly with increasing T. This tendency is in concordance with our previous observation. The calculated (↑) and (↓) k_e/τ are listed in Table 1.

3.2.2. Seebeck coefficient

The Seebeck coefficient (S) is an important quantity which is related to the electronic band structure of materials. The Seebeck coefficient of the β′-$Tb_2(MoO_4)_3$ at a certain value of chemical potential as a function of T is presented in Fig. 3(j). The sign of S indicates the type of dominant charge carriers; S with a positive sign represents the p-type materials, whereas n-type materials have negative S [30,50,51]. Following Fig. 3(j), it is clear that S has a negative value for (↑) and (↓), which confirms that the β′-$Tb_2(MoO_4)_3$ possesses n-type conductions at the vicinity of E_F. In further investigation, we calculated (↑)(↓)S as a function of $\mu - E_F = \pm 0.3$ eV at three constant T. In Fig. 3(k–m), we have illustrated S along the chemical potential between 0.3 and −0.3 eV. One can see in the vicinity of E_F that the (↑)(↓) S exhibit two pronounced structures just below and above E_F, with the highest value of S at 300 K (110.0 and −120.0 $\mu V/K$) for spin-up and (119.0 and −109.0 $\mu V/K$) for spin-down. It was noticed that at 300 K the (↓) shows a higher +S value than that of (↑), while for −S the (↑) shows a higher value than that for (↓). It is clear that with increasing T there is a significant reduction in the S value along $\mu - E_F = \pm 0.3$ eV . We should emphasize that with increasing T the (↓) shows lower +S and higher −S than that of (↑). The values of (↑)(↓) S at 300, 600 and 900 K are listed in Table 1.

3.2.3. Power factor

The power factor being defined as ($P = S^2\sigma/\tau$), it is clear that P is directly proportional to S^2 and σ/τ. Therefore, in order to gain high P one needs to maintain the values of S^2 and σ/τ. It is well known that the figure of merit is a very important quantity for calculating the transport properties of materials. The dimensionless figure of merit is written as ($ZT = S^2\sigma T/k$) [52,53], which shows that P comes in the numerator of the figure of merit; thus P is an important quantity and plays a principle role in evaluating the transport properties of the materials. We calculated the (↑)(↓) P of the β′-$Tb_2(MoO_4)_3$ at a certain value of chemical potential as a function of T, as shown in Fig. 3(n). It was found that the (↑) P is zero at low energies (∼50 K); then a rapid increase occurs when we raise T to reach its maximum value of about 0.5×10^{14} (W/mk^2s) at ∼150 K; then it reduces with further increase in T to reach the zero value at 900 K. Whereas the (↓) P has a value of about 2.3×10^{19} (W/mk^2s) at ∼50 K. Above 50 K, a sharp reduction occurs and P reaches its minimum value of about 0.3×10^{19} (W/mk^2s) at ∼200 K; then it drops to zero at 700 K. In order to ascertain the influence of varying the chemical potential on P, we calculated the (↑)(↓) P at three fixed values of T as a function of $\mu - E_F$ between −0.3 and +0.3 eV, as shown in Fig. 3(o–q). It was found that the investigated material exhibits the highest P just above and below E_F; it is interesting to see that increasing T causes a significant reduction in P and separates the two peaks which are located at E_F. The calculated values of the (↑)(↓) P at 300, 600 and 900 K in the vicinity of E_F are listed in Table 1. Based on the literature, the transport properties obtained from the BoltzTraP code agree well with the experimental data.

4. Conclusions

The (↑)(↓) transport properties of the spin-polarized β′-$Tb_2(MoO_4)_3$ are obtained from the band structure utilizing the semi-classical Boltzmann theory. The calculations of the transport properties is a transition from first- to second-principles methods. The first-principles method used here is FPLAPW+lo, whereas the second-principles method is the BoltzTraP code, which solves the semi-classical Bloch-Boltzmann transport equations. The calculated (↑)(↓) electronic band structure reveals that the β′-$Tb_2(MoO_4)_3$ has parabolic bands in the vicinity of E_F; therefore, the carriers exhibit low effective mass and hence high mobility. It has been found that the (↑)(↓) n increases linearly with increasing T and exhibits a maximum n at E_F. Calculations show that the β′-$Tb_2(MoO_4)_3$ exhibits maximum (↑)(↓) σ/τ, minimum (↑)(↓)k_e/τ, high (↑)(↓) S and high (↑)(↓)P at the vicinity of E_F. Therefore, the vicinity of E_F is the area where β′-$Tb_2(MoO_4)_3$ is expected to show maximum efficiency.

Acknowledgments

The result was developed within the CENTEM project, reg. no. CZ.1.05/2.1.00/03.0088, cofunded by the ERDF as part of the Ministry of Education, Youth and Sports OP RDI programme and, in the follow-up sustainability stage, supported through CENTEM PLUS (LO1402) by financial means from the Ministry of Education, Youth and Sports under the National Sustainability Programme I. Computational resources were provided by MetaCentrum (LM2010005) and CERIT-SC (CZ.1.05/3.2.00/08.0144) infrastructures.

References

[1] H.J. Borchardt, P.E. Bierstedt, J. Appl. Phys. 38 (1967) 2057–2060.
[2] A.K. Tripathi, H.B. Lal, J. Phys. Soc. Jpn. 49 (1980) 1896–1901.
[3] V.A. Efremov, Russ. Chem. Rev. 59 (1990) 627–642.

[4] V. Dmitriev, V. Sinitsyn, R. Dilanian, D. Machon, A. Kuznetsov, E. Ponyatovsky, G. Lucazeau, H.P. Weber, J. Phys. Chem. Solids 64 (2003) 307–312.
[5] B.G. Bazarov, R.F. Klevtsova, O.D. Chimitova, I.A. Glinskaya, K.N. Fedorov, Y.L. Tushinova, Z.G. Bazarova, Russ. J. Inorg. Chem. 51 (2006) 800–804.
[6] Z.G. Xia, D.M. Chen, J. Am. Ceram. Soc. 93 (2010) 1397–1401.
[7] M. Mączka, A. Majchrowski, I.V. Kityk, Vib. Spectrosc. 64 (2013) 158–163.
[8] O.D. Chimitova, V.V. Atuchin, B.G. Bazarov, M.S. Molokeev, Z.G. Bazarova, Proc. SPIE 8771 (2013) 87711A.
[9] J. Hanuza, L. Macalik, K. Hermanowicz, J. Mol. Struct. 319 (1994) 17–30.
[10] L. Macalik, J. Alloys Compd. 341 (2002) 226–232.
[11] A. Kato, S. Oishi, T. Shishido, M. Yamazaki, S. Iida, J. Phys. Chem. Solids 66 (2005) 2079–2081.
[12] O.D. Chimitova, B.G. Bazarov, R.F. Klevtsova, A.G. Anshits, K.N. Fedorov, A.V. Dubentsov, T.A. Vereshchagina, Y.L. Tushinova, L.A. Glinskaya, Z.G. Bazarova, et al., J. Struct. Chem. 51 (2010) 173–176.
[13] J.F. Tang, Y.J. Chen, Y.F. Lin, X.H. Gong, J.H. Huang, Z.D. Luo, Y.D. Huang, J. Opt. Soc. Am. B 27 (2010) 1769–1777.
[14] V.V. Atuchin, V.G. Grossman, S.V. Adichtchev, N.V. Surovtsev, T.A. Gavrilova, B. G. Bazarov, Opt. Mater. 34 (2012) 812–816.
[15] C.S. Lim, Asian J. Chem. 24 (2012) 5662–5664.
[16] V.V. Atuchin, O.D. Chimitova, S.V. Adichtchev, B.G. Bazarov, T.A. Gavrilova, M.S. Molokeev, N.V. Surovtsev, Zh.G. Bazarova, Mater. Lett. 106 (2013) 26–29.
[17] S. Mielcarek, Z. Tylczyński, Z. Trybuła, S. Łoś, B. Mroz, Cryst. Res. Technol. 40 (12) (2005) 1146–1149.
[18] Guipeng Cai, Jiyang Wang, Huaijin Zhang, Cryst. Res. Technol. 44 (9) (2009) 1001–1004.
[19] K. Nassau, H.J. Levinstein, G.M. Loiacono, J. Phys. Chem. Solids 26 (1965) 1805.
[20] Song Peng, Wei Cai, Xiaofei Wang, Yi Kan, Fengzhen Huang, Xu. Min, Huaijin Zhang, Jiyang Wang, Lu. Xiaomei, Jinsong Zhu, Ferroelectrics 410 (2010) 69–74.
[21] H.J. Borchardt, P.E. Bierstedt, J. Appl. Phys. 18 (1967) 2057–2060.
[22] E.T. Keve, S.C. Abrahams, K. Nassau, A.M. Glass, Solid State Commun. 8 (1970) 1517–1520.
[23] E.T. Keve, S.C. Abrahams, J.L. Berstein, J. Chem. Phys. 54 (1971) 3185–3194.
[24] S.C. Abrahams, C. Svensson, J.L. Bernstein, J. Chem. Phys. 72 (1980) 4278–4285.
[25] C. Svensson, S.C. Abrahams, J.L. Bernstein, J. Chem. Phys. 71 (1979) 5191–5195.
[26] H. Ida, K. Shinozaki, T. Honma, K. Oh-ishi, T. Komatsu, J. Solid State Chem. 196 (2012) 384.
[27] M. Imaoka, J. Ceram. Soc. Japan 69 (1961) 282.
[28] A.H. Reshak, Eur. Phys. J. B 89 (2016) 256.
[29] P. Blaha, K. Schwarz, G. K. H. Madsen, D. Kvasnicka, J. Luitz, WIEN2k, An augmented plane wave plus local orbitals program for calculating crystal properties, Vienna University of Technology, Austria (2001).
[30] G.K.H. Madsen, D.J. Singh, Comput. Phys. Commun. 175 (2006) 67–71.
[31] V.V. Atuchin, A.S. Aleksandrovsky, O.D. Chimitova, A.S. Krylov, M.S. Molokeev, B.G. Bazarov, J.G. Bazarova, Zhiguo Xia, Opt. Mater. 36 (2014) 1631–1635.
[32] E.T. Keve, S.C. Abrahams, J.L. Bernstein, J. Chem. Phys. 54 (1971) 3185.
[33] F.G. Ulman, B.J. Holden, B.N. Gauguly, J.R. Hardy, Phys. Rev. B 8 (1973) 2991.
[34] S.S. Saleem, G. Arulhas, H.D. Bist, J. Solid State Chem. 48 (1983) 77.
[35] L. Guy, M. Denis, J. Raman Spectrosc. 37 (2006) 189.
[36] Wu. Fang, Hong zhang Song, Jian feng Jia, , , Progress in Natural Science: Materials International 23 (4) (2013) 408–412.
[37] J.P. Perdew, S. Burke, M. Ernzerhof, Generalized gradient approximation made simple, Phys. Rev. Lett. 77 (1996) 3865.
[38] V.I. Anisimov, I.V. Solvyev, M.A. Korotin, M.T. Czyzyk, C.A. Sawatzky, Phys. Rev. B 48 (1993) 16929.
[39] A.I. Liechtenstein, V.I. Anisimov, J. Zaanen, Phys. Rev. B 52 (1995) R5467.
[40] O.K. Andersen, Phys Rev B 12 (1975) 3060.
[41] J.P. Perdew, Y. Wang, Phys Rev B 45 (1992) 13244.
[42] S. Hardev Saini, Mukhtiyar Singh, A.H. Reshak, „ J. Magn. Magn. Mater. 331 (2013) 1–6.
[43] A.H. Reshak, H. Kamarudin, Z.A. Alahmed, S. Auluck, Jan Chyský, J. Magn. Magn. Mater. 361 (2014) 206–211.
[44] Y. Saeed, S. Nazir, A. Shaukat, A.H. Reshak, J. Magn. Magn. Mater. 322 (2010) 3214–3222.
[45] B.K. Ponomarev, B.S. Red'kin, A.G.M. Jansen, P. Wyder, H. Wiegelmann, E. Steep, Phys. Solid State 50 (2008) 1495–1501.
[46] M. Xu, Y.G. Yu, H.J. Zhang, J.Y. Wang, J. Rare Earths 27 (2009) 192–195.
[47] G.P. Cai, J.Y. Wang, H.J. Zhang, Cryst. Res. Technol. 44 (2009) 1001–1004.
[48] S. Peng, W. Cai, X.F. Wang, Y. Kan, F.Z. Huang, M. Xu, H.J. Zhang, J.Y. Wang, X.M. Lu, J.S. Zhu, Ferroelectrics 410 (2011) 69–74.
[49] G.J. Snyder, E.S. Toberer, Nat. Mater. 7 (2008) 105–114.
[50] B. Xu, X. Li, G. Yu, J. Zhang, S. Ma, Y. Wang, L. Yi, J. Alloys Compd. 565 (2013) 22–28.
[51] T.J. Scheidemantel, C. Ambrosch-Draxl, T. Thonhauser, J.V. Badding, J.O. Sofo Phys. Rev. B 68, 2003, 125210(6).
[52] Chenming Calvin Hu, Modern Semiconductor Devices for Integrated Circuits, Part I: Electrons and holes in a semiconductor November 11, 2011
[53] Joo-Hyoung Lee, Wu. Junqiao, Jeffrey C. Grossman, PRL 104 (2010) 016602.